

# Magic State Injection on IBM Quantum Processors Above the Distillation Threshold

Younghun Kim,<sup>1,2,\*</sup> Martin Sevier,<sup>1</sup> and Muhammad Usman<sup>1,2,†</sup>

<sup>1</sup>*School of Physics, The University of Melbourne, Parkville, 3010, Victoria, Australia*

<sup>2</sup>*Data61, CSIRO, Clayton, 3168, Victoria, Australia*

The surface code family is a promising approach to implementing fault-tolerant quantum computations by providing the desired reliability via scaling the code size. For universal fault-tolerance requiring logical non-Clifford quantum operations in addition to Clifford gates, it is imperative to experimentally demonstrate the implementation of additional resources known as magic states, which is a highly non-trivial task. Another key challenge is efficient embedding of surface code in quantum hardware layout to harness its inherent error resilience and magic state preparation techniques, which becomes a difficult task for hardware platforms with connectivity constraints. This work simultaneously addresses both challenges by proposing a qubit-efficient rotated heavy-hexagonal surface code embedding in IBM quantum processors (`ibm_fez`) and implementing the code-based magic state injection protocol. Our work reports error thresholds for both logical bit- and phase-flip errors, obtaining  $\approx 0.37\%$  and  $\approx 0.31\%$ , respectively, which are higher than the threshold values previously reported with traditional embedding. The post-selection-based preparation of logical magic states  $|H_L\rangle$  and  $|T_L\rangle$  achieve fidelities of  $0.8806 \pm 0.0002$  and  $0.8665 \pm 0.0003$ , respectively, which are both above the magic state distillation threshold. Additionally, we report the minimum fidelity among injected arbitrary single logical qubit states as  $0.8356 \pm 0.0003$ . Our work demonstrates the potential for implementing non-Clifford logical gates by producing high-fidelity logical magic states on IBM quantum devices.

## I. INTRODUCTION

Quantum error correction is vital to achieve scalable and universal fault-tolerant quantum computation by suppressing inevitable errors in contemporary quantum computing [1–4]. Surface codes have emerged as one of the leading quantum error correction protocols, which promise to protect quantum information by encoding it across highly entangled many-body qubits [5–8]. Their crucial properties are stabilizing qubits and discretizing errors into relatively easy-to-correct forms while requiring a straightforward coupling map [9]. In recent years, surface code implementations, albeit on a small scale, have been demonstrated on a variety of quantum hardware platforms such as superconducting [10–13], trapped ion systems [14], and neutral atom systems [15]. However, the research on experimental surface code implementations is at the preliminary stages and a universal fault-tolerant quantum computing is still an open problem that will require a demonstration of surface code protected universal gate set including both Clifford and non-Clifford quantum operations [16–18].

Although the experimental demonstration of Clifford gates with surface code formalism and its variants has been quite successful in the literature [15, 19–25], it is well known theoretically that the implementation of non-Clifford operations is a highly nontrivial task that requires employing a specific logical qubit state, known as a logical magic state [19, 26]. Therefore, the experimental realization of the logical magic state is an important milestone towards achieving universal quantum

computing [27–30], which is still a subject of ongoing endeavor. To our knowledge, only a couple of experimental studies [29, 30] to date have recently reported the preparation of magic states using surface codes. While Ref. [29] has shown distance-3 implementations exceeding the distillation threshold value for square lattice code, the study in Ref. [30] was only distance-2 surface codes without scaling, reporting limited scope of magic state injection on heavy-hexagonal architecture. In this work, we report the first distance-3 implementations of surface code-based magic state injection on one of IBM quantum processors and demonstrate that any arbitrary single logical qubit state, including the logical magic states above the distillation threshold, can be prepared. We note here that while the previous study [29] was based on a square grid lattice of qubits, our work has performed rotated surface code embedding in the heavy-hexagonal architecture of IBM quantum processors. This is also the first such implementation on IBM devices which reduces physical qubit requirements to approximately half for a logical qubit implementation compared to previous surface code embeddings [31, 32], therefore opening the possibility for significantly reducing the resource requirements for scalable surface code implementations.

This work proposes and implements a scheme for preparing arbitrary logical qubit states on a heavy-hexagon lattice. This scheme utilizes a rotated surface code tailored to the lattice’s structure. We layout the procedure for embedding the rotated surface code and the code-based magic state injection protocol. The proposed code exhibits a relatively high threshold compared to other lattice-compatible codes [32–35], obtaining  $\approx 0.37\%$  and  $\approx 0.31\%$  threshold values for both logical bit- and phase-flip errors, respectively. Additionally, we conduct magic state injection experiments using distance-

\* [younghunk@student.unimelb.edu.au](mailto:younghunk@student.unimelb.edu.au)

† [muhammad.usman@unimelb.edu.au](mailto:muhammad.usman@unimelb.edu.au)

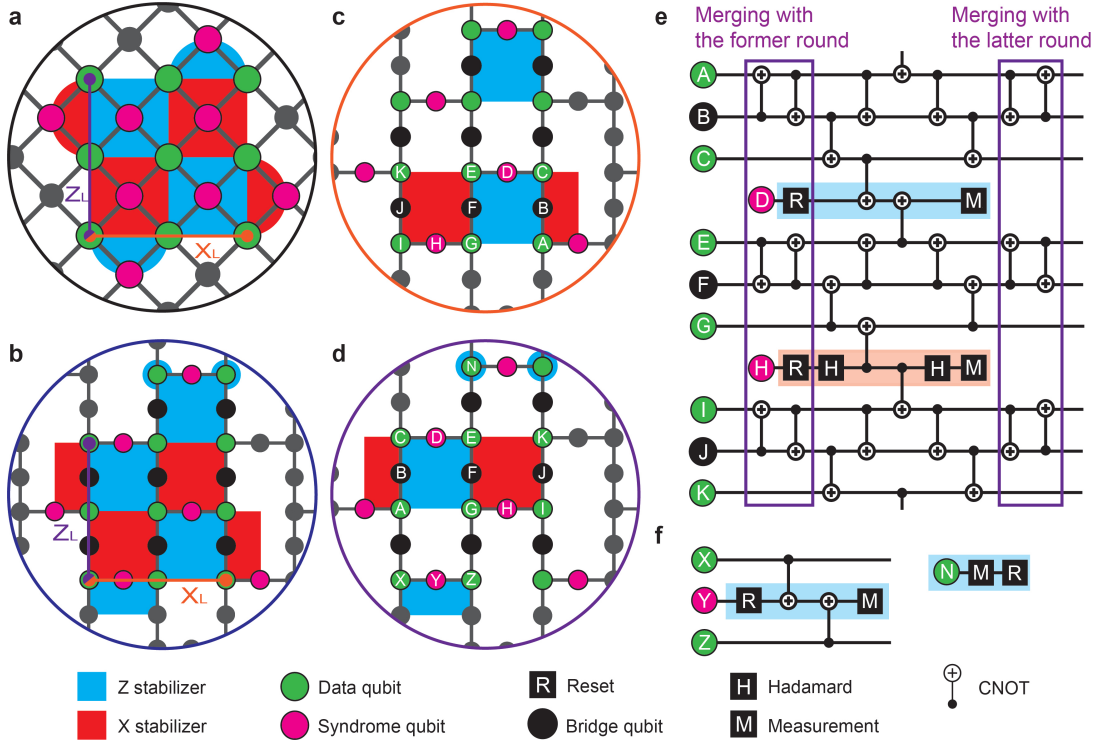


FIG. 1: **Embedding rotated surface code.** **a,b.** Qubit arrangements of the rotated surface code in the square and heavy-hexagon lattices. The logical Z and X operators are represented by the purple and orange solid lines, respectively. **c,d.** The stabilizers of the code are divided into two sub-groups. **e.** A sub-round syndrome extraction circuit measures weight-four stabilizers including those at the side boundaries within the same sub-group. The first and last two layers of CNOT gates can be executed in parallel along with the former and latter sub-rounds. **f.** Subroutine circuits for measuring weights-two and -one Z stabilizers at top and bottom boundaries.

3 codes on `ibm_fez` device. Our circuit can encode any arbitrary single-qubit state into the logical qubit state of the code. Among logically encoded states, the logical magic states relevant for the non-Clifford quantum operations namely  $|H_L\rangle$  and  $|T_L\rangle$  are prepared with fidelities of  $0.8806 \pm 0.0002$  and  $0.8665 \pm 0.0003$ , respectively, both exceeding their distillation threshold values.

## II. ROTATED SURFACE CODE EMBEDDING

The rotated surface code is an optimized variant of the conventional surface code that reduces the qubit requirement to half while preserving code distance by using a different orientation of the qubit arrangement. Although previous work has addressed surface code implementation in a heavy-hexagon lattice [32], embedding its rotated version remains unresolved. This work investigates the feasibility and efficiency of embedding the rotated surface code with respect to the connectivity limitations. We will estimate its threshold value for logical Pauli errors as scaling the code distance, along with the demonstration of encoding logical magic states to reduce qubit requirements by exploiting the rotated version of surface codes on one of IBM's devices.

In a square lattice, the rotated surface code displayed in Fig. 1a can concurrently stabilize data qubits in a subspace that yields +1 Eigen values for its stabilizer group. The stabilizer group includes weight-four at the bulk and weight-two stabilizers at the boundaries, defined with commutable multi-qubit Pauli operators. However, the limited connectivity of the heavy-hexagon lattice makes embedding of rotated code a challenging task. This is because each qubit has at most three neighbors instead of four, which limits measuring weight-four stabilizers in the same manner as on the square lattice. The rotated surface code can be embedded in the heavy-hexagon lattice, as shown in Fig. 1b, by stabilizing data qubits through two consecutive sub-rounds. Each sub-round measures the corresponding subgroup stabilizers, as illustrated in Fig. 3c, and d.

$$\hat{Z}_A \hat{Z}_C \hat{Z}_E \hat{Z}_G \xrightleftharpoons[\text{unfold}]{\text{fold}} \hat{Z}_C \hat{Z}_E \quad (1a)$$

$$\hat{X}_E \hat{X}_G \hat{X}_I \hat{X}_K \xrightleftharpoons[\text{unfold}]{\text{fold}} \hat{X}_G \hat{X}_I \quad (1b)$$

The key idea behind measuring weight-four stabilizers, such as  $\hat{Z}_A \hat{Z}_C \hat{Z}_E \hat{Z}_G$  and  $\hat{X}_E \hat{X}_G \hat{X}_I \hat{X}_K$ , while respecting connectivity limitation is transforming them into

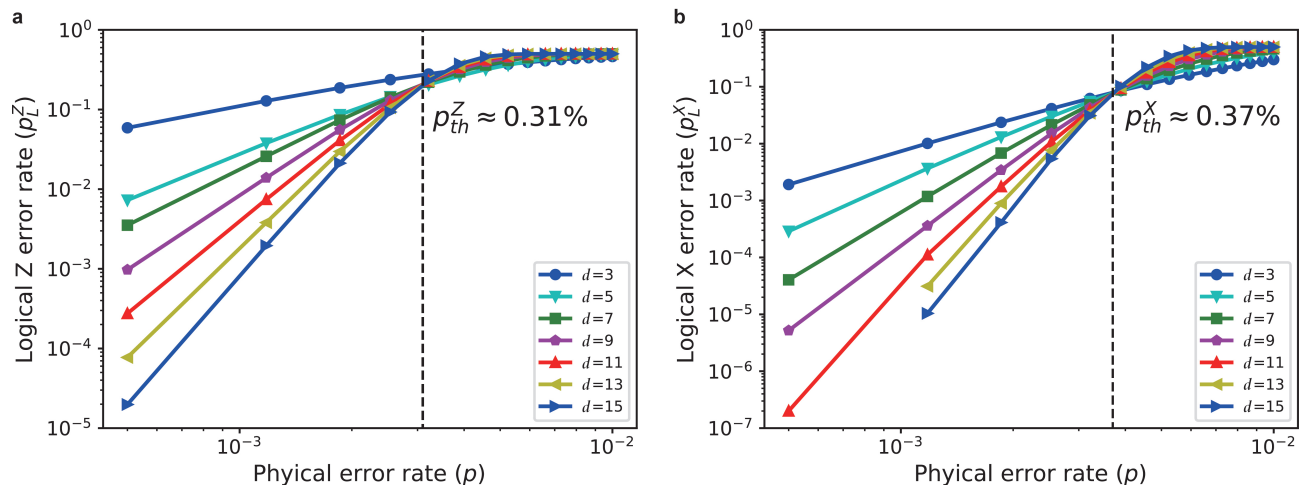


FIG. 2: **Logical error rates.** **a,b.** Logical Z and X error rates as functions of the code distance, denoted as  $d$ , and the physical error rate ( $p$ ), showing error suppression via scaling code size. While the code distance ranges from 3 to 15, the physical error rate  $p$  varies from  $5 \times 10^{-4}$  to  $10^{-2}$ . The logical error rates are calculated using  $5 \times 10^6$  samples. The threshold values are obtained as  $p_{\text{th}}^Z \approx 0.31\%$  and  $p_{\text{th}}^X \approx 0.37\%$  for logical Z and X errors, respectively.

weight-two stabilizers, in other words, folding stabilizers. The folded stabilizers are then measured using syndrome qubits to extract their eigenvalues. Following measurement, the original stabilizers are restored by reversing the series of quantum gates applied during the folding process, which is unfolding stabilizers. Fig. 1e shows a sub-round syndrome extraction circuit for the measurement of weight-four stabilizers following the process of (un)folding stabilizers as expressed in (1a) and (1b). The circuit requires long-range interactions between data qubits, which can be effectively done using bridge qubits as intermediates. To optimize the circuit, the first and last two layers of CNOT gates in the former and latter sub-rounds are applied simultaneously to minimize the circuit depth across sub-rounds.

While the stabilizers at the side boundaries can also be measured with those at the bulk, the stabilizers at the top or bottom boundaries need to be measured as weight-two and -one stabilizers as illustrated in Fig. 1f. For the Z stabilizers at the bottom boundary, the two-weight stabilizers can be directly measured using the syndrome qubits. Concerning those at the top boundary, we update the stabilizer group by measuring weight-four or weight-one stabilizers, such as  $\hat{Z}_N$ , as sub-rounds executed alternatively. The measurement of the weight-one stabilizers collapses the corresponding data qubit states, allowing the remaining data qubits to span the code space where qubit information is protected from errors. Since the measurement of these stabilizers does not involve bridge qubits, they require relatively few time steps compared to those required for weight-four. However, we simultaneously apply measurements for stabilizers in the same sub-round regardless of their weight.

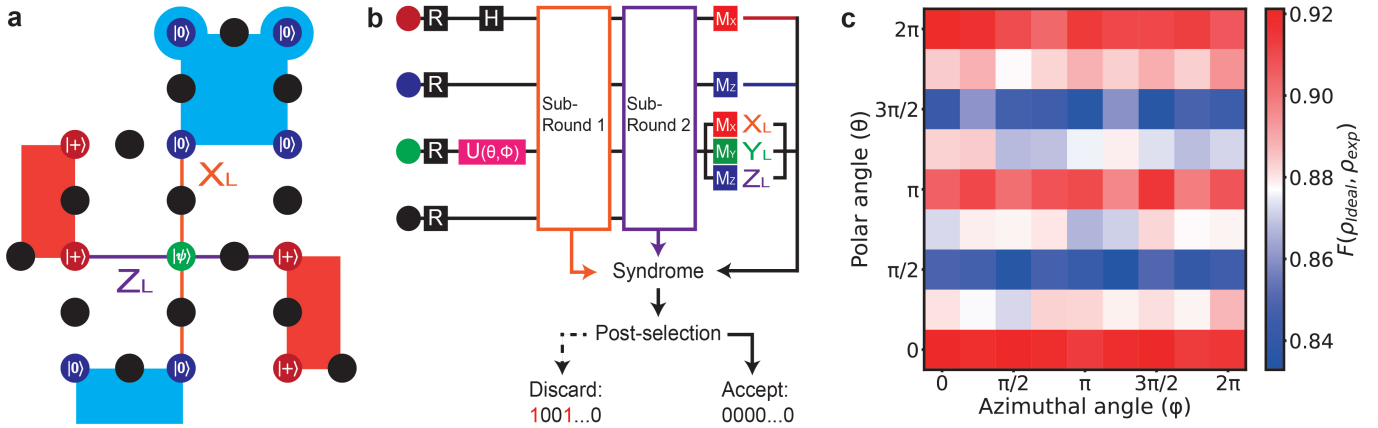
For evaluating the proposed code, we computed logical error rates as a function of the physical error rates under the circuit-level uniform noise model (the details are in

TABLE I: **Qubit requirements.** The required number of physical qubits for embedding rotated and unrotated surface codes on the heavy-hexagon lattice as a function of the code distance ( $d$ ).

	Unrotated	Rotated
# of data qubits	$2d^2 - 1$	$d^2 + d - 1$
# of qubits	$5d^2 - 2(d + 1)$	$5/2d^2 + 2d - 7/2$

Methods). Fig. 2a and b show the logical error rates for the two states, either in the X ( $|+_L\rangle$ ) basis or in Z ( $|0_L\rangle$ ) basis, corresponding to the probability of logical Z and X errors, respectively. The logical error rates are calculated under various physical error rates ( $p$ ) ranging from  $5 \times 10^{-4}$  to  $10^{-2}$  and code distances ( $d$ ) ranging from 3 to 15. Although the number of qubits required for the rotated code scales with the code distance as  $O(d^2)$ , the same as for its unrotated version, the former requires about half the number of qubits in the limit of large code distances. The number of qubits as a function of the code distance is listed in Table I.

We obtain the threshold values for logical phase- and bit-flip errors as  $\approx 0.31\%$  and  $\approx 0.37\%$ , respectively. Although its unrotated version has a threshold of  $0.3\%$  [32], the highest among other lattice-compatible codes suggested so far, we find that the proposed code in this work achieves a slightly even higher threshold value for both error types. Notably, we observe a faster improvement in performance for bit-flip error corrections compared to phase-flip error corrections as the physical error rate decreases below the threshold, given the same code distance. Additionally, the threshold value for a logical Z error is smaller than that for a logical X error. This indicates an asymmetric feature, that has not been observed in the square lattice, in correcting the two types



**FIG. 3: Magic state injection and implementation.** **a.** The initialization layout for magic state injection utilizing the embedded rotated surface code. Each data qubit is initialized with the ground state in either the Z basis ( $|0\rangle$ ), represented as blue nodes, or the X basis ( $|+\rangle$ ), represented as red nodes. The central data qubit, magic state, is prepared in the state  $|\psi\rangle$  and depicted as a green node. **b.** The data qubits are initialized according to the layout, employing a single-qubit unitary operation ( $U$ ) for the magic state. Following that, two consecutive sub-round syndrome extraction circuits are executed. The magic state is measured in the basis determined by the logical Pauli measurement, while the remaining data qubits are measured in the same basis as their initialization. The outcomes are used to detect errors and discard non-trivial syndromes through post-selection. **c.** The fidelities of raw logical magic states prepared using the circuit **b** are plotted on a plane with the polar ( $\theta$ ) and azimuthal ( $\phi$ ) angles, ranging from 0 to  $2\pi$ . The values are estimated from the trivial syndromes obtained by sampling  $2 \times 10^4$  times for logical measurements in each Pauli basis.

of errors under the unbiased noise model when rotating the embedded code in the heavy-hexagon structure. More details about the feature are discussed in Appendix A.

### III. MAGIC STATE INJECTION PROTOCOL

We next discuss a code-based magic state injection protocol. The protocol consists of four main steps: 1. Initialization, 2. Stabilizer measurement, 3. Logical Pauli measurement, and 4. Post-selection.

1. Initialization: Data qubits are prepared in their designated quantum states, as depicted in Fig. 3a. These states include the ground state of the Z basis ( $|0\rangle$ ) or the X basis ( $|+\rangle$ ). Additionally, the central qubit, the magic state, is prepared as  $|\psi\rangle = \cos(\theta/2)|0\rangle + e^{i\phi}\sin(\theta/2)|1\rangle$ , intended for injection at the logical qubit level, using a primitive single-qubit gate parameterized with  $\theta$  and  $\phi$ .
2. Stabilizer measurement: Two sub-rounds of syndrome extraction circuits are performed and measure full stabilizers.
3. Logical Pauli measurement: As shown in Fig. 3b, the central data qubit is measured in the same Pauli basis as the interested logical Pauli measurement basis either X, Y, or Z. In contrast, the remaining data qubits are measured in the same basis as initialized.

4. Post-selection: Based on the measured outcomes, we evaluated deterministic parity values described in 4a and 4b, turning into a syndrome. When there is an error, it produces a non-trivial syndrome which will be discarded, as shown in Fig. 3b.

- (a) The measurement outcomes from the sub-round syndrome extraction circuits align with the initially conditioned stabilizers at the boundaries.
- (b) The parity of the measurements for the data qubits associated with the boundary stabilizers matches the eigenvalue of the corresponding stabilizer.

We decided to design the protocol using a distance-3 rotated surface code, which reduces the number of qubits by one-third compared to its unrotated version. The reduced qubit requirement not only minimizes the sources of errors but also increases the success rate for the post-selection in experiments.

Initialized data qubits satisfy the condition of having +1 eigenvalues at all boundary stabilizers. In the absence of noise, even after the sub-round syndrome extraction circuits have been executed, initially stabilized eigenvalues remain deterministic and unchanged. These measured outcomes result in a logically encoded state  $|\psi_L\rangle = \cos(\theta/2)|0_L\rangle + e^{i\phi}\sin(\theta/2)|1_L\rangle$  with predefined parameters  $\theta$  and  $\phi$ . Additionally, the measured data qubits also align with these initial conditions. Finally, the logical Pauli measurement is determined by the parity of the



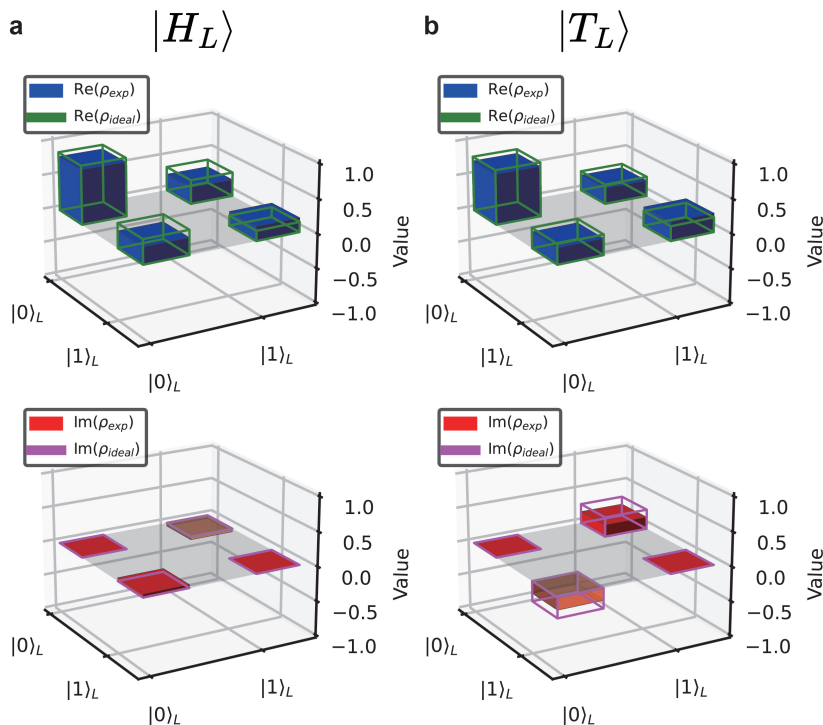


FIG. 4: **Density matrices of logical magic states. a,b.** The real and imaginary values of the density matrices for the ideal and experimental results are plotted for  $|H_L\rangle$  and  $|T_L\rangle$ , with ideal values represented by lines and experiment values by bars. A grey plane indicates the region where the value is 0.

measured outcomes from data qubits associated with the target logical operator [29]. The projective logical Pauli measurement can be altered in its basis depending on experiments.

We conducted experiments using 25 physical qubits on `ibm_fez` quantum device, one of IBM’s quantum processors, accessed via the cloud. The experiments were conducted using the parameters  $\theta$  and  $\phi$  ranging from 0 to  $2\pi$  in  $\pi/4$  intervals. The details on the preparation of an arbitrary magic state ( $|\psi\rangle$ ) through a primitive single-qubit gate are provided in Methods. Each logical Pauli measurement for the X, Y, and Z basis is repeated  $2 \times 10^4$  times per state with a sample taking approximately  $6.8\mu s$ .

It is worth discussing the error rates of logic quantum gates in particular two-qubit gates and measurements on the hardware. During our experiments, the average error rate from two-qubit gates ( $2.9 \times 10^{-3}$ ) was below the threshold values for both types of logical errors of the code. In contrast, the same for the readout case ( $1.6 \times 10^{-2}$ ) was an order of magnitude higher compared to the threshold values. Further details of the error rates can be found in the Methods. Although this might lead logical qubits susceptible to measurement-induced logical errors more than gate-induced ones, the post-selection in the experiments could effectively detect both measurement-induced and gate-induced errors during error detection, potentially improving the fidelity of logical magic states. As a result, the average acceptance rate

was  $36.28 \pm 0.09\%$  of runs for each logical Pauli measurement in disagreement with the post-selection criteria. In Methods, we show the acceptance rates of post-selection in Eigen states of logical Pauli operators.

$$F(\rho_{\text{ideal}}, \rho_{\text{exp}}) = \left( \text{Tr} \left( \sqrt{\sqrt{\rho_{\text{exp}}} \rho_{\text{ideal}} \sqrt{\rho_{\text{exp}}}} \right) \right)^2 \quad (2)$$

Based on the post-selected samples from the experiments on the IBM device, we calculate fidelities for logical qubit states. The fidelities are calculated between the ideal ( $\rho_{\text{ideal}}$ ), and experimentally reconstructed density matrix ( $\rho_{\text{exp}}$ ) as expressed in equation (2). While the ideal density matrix is obtained from the theoretical logical qubit state as  $\rho_{\text{ideal}} = |\psi_L\rangle\langle\psi_L|$ , the experimental density matrix is estimated based on the expectation values from the logical Pauli operators (see Methods). Additionally, we compare theoretical and experimental logical Pauli expectation values in Appendix B.

In Fig. 3c, we plot the fidelities for the experimentally encoded logical qubit states. When the polar angle ( $\theta$ ) is an integer multiple of  $\pi$  regardless of the azimuthal angle ( $\phi$ ), logical qubits are prepared in the Eigen states of the logical Z operator where the values are prominently high. However, we observe a gradual decrease in the fidelities of qubit states, when the state is placed in the superposition of two computational Z basis states with different phases and is injected. Under the assumption that primitive gates in the hardware have no biased noise, we

attribute the relative vulnerability of phase information to the inherent bias of the resilience of the code against bit-flip errors. This aligns with the asymmetric feature of the code analyzed theoretically. Additionally, the minimum value has been found in the Y basis state with +1 Eigen value from the logical Y operator as  $0.8356 \pm 0.0003$  where the state is susceptible to both bit-flip and phase-flip errors. However, even with anti-symmetrical robustness against errors, we note that our protocol achieves an average fidelity of  $0.882 \pm 0.006$ .

Finally, we test our model in the preparation of well-known logical magic states,  $|H\rangle = \cos(\pi/8)|0\rangle + \sin(\pi/8)|1\rangle$  and  $|T\rangle = \cos(\beta)|0\rangle + e^{i\pi/4}\sin(\beta)|1\rangle$ , where  $\cos(2\beta) = 1/\sqrt{3}$ . H- and T-type states can be used to realize phase-shift gates, which belong to non-Clifford gates [26]. The threshold fidelity values of  $|H\rangle$ , using a 7-to-1 distillation routine [16], and  $|T\rangle$ , using a 5-to-1 distillation routine [26], are 0.854 and 0.827.

We conduct experiments to prepare the magic states and analyze their fidelities. These results are shown in Fig. 4a and b to compare the ideal and experimental density matrices for the two logical magic states. The fidelity of the logical magic states,  $|H_L\rangle$  and  $|T_L\rangle$ , are prepared with the fidelity  $0.8806 \pm 0.0002$  and  $0.8665 \pm 0.0003$ , respectively, above their threshold for distillation protocol. The uncertainty of fidelities is estimated using a bootstrapping technique (see Methods).

#### IV. CONCLUSION AND DISCUSSION

In this work, we demonstrate the preparation of an arbitrary encoded logical single-qubit state using a compatible rotated surface code on `ibm_fez` quantum processor. First, we propose a rotated surface code, which requires around half the number of qubits as its unrotated version for large code distances, in the heavy-hexagon structure. We compute the threshold values of the code and find its asymmetric feature in error correction. Furthermore, we have achieved high fidelity from the injection protocol implemented on the arbitrary single-qubit states in logical encoding on the IBM device. We also realize two logical magic states  $|H_L\rangle$  and  $|T_L\rangle$  type, which are of high relevance for implementing non-Clifford gates for quantum error correction, that exceed the threshold fidelity of magic state distillation on IBM hardware.

Several challenges remain to achieve the universality of the logical quantum gate set; however, our work marks an important step towards universal quantum computing by demonstrating the preparation of raw logical magic states on one of IBM quantum devices. For future work, it would be intriguing to conduct quantum memory experiments and demonstrate error suppression using our scheme, which can be configured with code distances varying from 3 to 5, and even 7 by shaping the code as a rectangular, on 156 physical qubit devices. Furthermore, increasing the size of the logical magic states and implementing lattice surgery would be another promis-

ing avenue for future work. In summary, our protocols pave the way for promising near-term advancements in quantum error codes for quantum hardware with connectivity constraints such as the heavy-hexagon structure employed by the IBM quantum processors.

#### V. METHODS

**Noise Model:** We evaluate threshold values of the rotated surface code embedded in the heavy-hexagonal structure under a circuit-level noise model. We adopt the noise model that decomposes error channels using Pauli operators. A depolarizing error channel is used, where errors are not biased but have uniform probabilistic distribution among Pauli errors [36]. When the error rate is  $p$ , the circuit-level noise model consists of the following noisy channels:

- **Single-Qubit Depolarizing Error Channel:** A single-qubit subjected to the error channel experiences Pauli errors ( $\hat{X}$ ,  $\hat{Y}$ , and  $\hat{Z}$ ) with equal probabilities. The error probabilities for  $\hat{X}$ ,  $\hat{Y}$ , and  $\hat{Z}$  are denoted by  $p_X$ ,  $p_Y$ , and  $p_Z$ , respectively, satisfying the condition  $p_X = p_Y = p_Z = p/3$ . This occurs when a physical qubit is inactive undergoing free evolution or when a single-qubit gate, such as  $\hat{H}$  is applied.
- **Initialization and Measurement Error Channel:** A bit-flip error, with the probability of  $p$ , is applied before measurement ( $M$ ) and after the reset gate in the Z basis ( $R$ ).
- **Two-Qubit Depolarizing Error Channel:** Two qubits are susceptible to Pauli errors when a two-qubit gate (CNOT) is applied. These Pauli errors from two qubits are represented by the set  $\{\hat{X}, \hat{Y}, \hat{Z}, \hat{I}\}^{\otimes 2} / \{\hat{I} \otimes \hat{I}\}$ . The probability of each error is uniform as  $p/15$ .

**Calculating Threshold:** In this work, to compute a logical error rate, we turn measured outcomes from syndrome extraction circuits into a syndrome to detect errors and use it to calculate a correction operator. Errors are detected through flipped measurement outcomes from the same syndrome qubits, which will produce “1” bits in the syndrome indicating the presence of errors, between the circuit rounds for weight-four and -two stabilizers. On the other hand, outcomes from weight-one stabilizers are directly used to detect errors. We utilize the open-source software tool Stim to generate syndrome samples using sub-round syndrome extraction circuits under circuit-level noise, where noise is decomposed as probabilistic Pauli gates [37]. Additionally, we use Py-matching to determine a correction operator as the most likely error based on the noise model [38, 39]. A logical error rate is computed as the ratio of the average number

of rounds to have a logical error for varying error rates and code distances.

**IBM Hardware:** We conducted the experiments on 31st October 2024, utilizing 25 out of 156 physical qubits on `ibm_fez` device. Measurement and two-qubit gate (CZ gate) error rates may vary per qubit within the device’s configuration. The error rates for the chosen qubits in the experiments are the hardware’s calibration data and are illustrated in Appendix Fig 6. The average error rates for readout and two-qubit gates were  $1.6 \times 10^{-2}$  and  $2.9 \times 10^{-3}$ , respectively.

**Implementation of the experiment:** We conducted optimized quantum circuits for the magic state injection protocol on the hardware. First, to optimize circuits, data qubits forming weight-one stabilizers are measured only once rather than twice, because there are redundant measurements of data qubits in the second sub-round syndrome extraction circuit and logical Pauli measurement. Second, we applied classically controlling X gates based on measurement outcomes of qubits to reset physical qubits [40]. This approach reduced the duration of implementing syndrome extraction circuits by minimizing the time for resetting qubits. Additionally, dynamic decoupling was applied to the physical qubits when they were inactive to minimize unwanted perturbations during quantum operations, including measurements [41].

We used a U3 gate to rotate a single-qubit to prepare  $|\psi\rangle$  state from the ground state ( $|0\rangle$ ), where the gate takes three parameters  $\theta$ ,  $\phi$ , and  $\lambda$ . The gate represents:

$$U3(\theta, \phi, \lambda) = \begin{pmatrix} \cos(\theta/2) & -e^{i\lambda}\sin(\theta/2) \\ e^{i\phi}\sin(\theta/2) & e^{i(\phi+\lambda)}\cos(\theta/2) \end{pmatrix}$$

, where we have set  $\lambda = 0$ . We employed the Python library Qiskit to transpile circuits into the device’s basis gates, enabling the execution of quantum circuits on the hardware [42].

**Qubit Tomography:** Any single-qubit density matrix ( $\rho$ ) can be written in terms of its Pauli operators  $\vec{\sigma} = (\hat{X}, \hat{Y}, \hat{Z})$  and the identity operator ( $\mathbb{1}$ ), such that:

$$\rho = \frac{1}{2}(\mathbb{1} + \vec{\sigma} \cdot \vec{r}) = \begin{pmatrix} 1-z & x-iy \\ x+iy & 1+z \end{pmatrix} \quad (3)$$

, where  $\vec{r} = (x, y, z)$  is a real vector representing the Bloch coordinates of  $\rho$ . The Bloch vector corresponds to the coefficients of each Pauli operator and can be used to reconstruct the density matrix. A single-qubit tomography is a process to estimate the Bloch vector based on the outcomes of non-commuting observables. The simplest method, direct inversion tomography, repeatedly measures a qubit state in the Pauli bases and obtains the expectation value for each basis, reconstructing the density matrix of the target single-qubit state [43].

The numbers of repeated measurements along the logical Pauli X, Y, or Z basis can be denoted by  $N_X$ ,  $N_Y$ , and  $N_Z$ , respectively. Each measurement yields one of

two outcomes: “up-state” with a +1 Eigen value for the corresponding Pauli operator, or the “down-state” corresponding to a -1 Eigen value. The counts of the up- and down-states are represented as  $N_{up}$  and  $N_{down}$  and their sum is the total number of measurements for a particular Pauli basis. For example,  $N_Z = N_{|0\rangle} + N_{|1\rangle}$ , and similarly for the other Pauli bases,  $N_X$  and  $N_Y$ . Based on these measured outcomes, the Bloch vector ( $\vec{r}_{\text{exp}}$ ) can be estimated by the expectation value of each Pauli operator as follows [43]:

$$\vec{r}_{\text{exp}} = \left( \frac{N_{|+\rangle} - N_{|-\rangle}}{N_X}, \frac{N_{|+i\rangle} - N_{|-i\rangle}}{N_Y}, \frac{N_{|0\rangle} - N_{|1\rangle}}{N_Z} \right) \quad (4)$$

TABLE II: Acceptance rates of post-selection in different Pauli bases, where  $N = 2 \times 10^4$ .  $N_X$  is the number of samples passed the post-selection for measuring logical X measurement. Likewise for  $N_Y$  and  $N_Z$ .

Logical state	$N_X/N$	$N_Y/N$	$N_Z/N$
$ 0\rangle_L$ ( $\theta = 0, \phi = 0$ )	0.3643	0.3704	0.3619
$ 1\rangle_L$ ( $\theta = \pi, \phi = 0$ )	0.3643	0.3685	0.3548
$ +\rangle_L$ ( $\theta = \pi/2, \phi = 0$ )	0.3581	0.3615	0.3511
$ -\rangle_L$ ( $\theta = \pi/2, \phi = \pi$ )	0.3713	0.3674	0.3677
$ +i\rangle_L$ ( $\theta = \pi/2, \phi = \pi/2$ )	0.3616	0.3715	0.3633
$ -i\rangle_L$ ( $\theta = \pi/2, \phi = 3\pi/2$ )	0.3669	0.3734	0.3613

As mentioned in the main paper, logical Pauli measurements are repeated  $2 \times 10^4$  per injected magic state. We discard any sample which has a non-trivial syndrome, it may vary the number of samples for  $N_{up}$  and  $N_{down}$  states. The acceptance rates of experimental results for the Eigen states of Pauli operators are listed in Table II. The samples that passed the post-selection are then used to calculate expectation values of logical Pauli operators corresponding to logical magic states.

**Bootstrapping:** The confidence intervals in experimental data are estimated using a bootstrapping method [44]. We classically resampled using the probability distribution obtained from the experiments.

## ACKNOWLEDGMENT

YK acknowledges the support of the CSIRO Research Training Program Scholarship and the University of Melbourne Research Training Scholarship. The University of Melbourne supported the research through the establishment of the IBM Quantum Network Hub.

## DATA AVAILABILITY

All datasets are available in the manuscript figures. Further data and source code can be made available upon reasonable request to the corresponding authors.

## AUTHOR CONTRIBUTIONS

YK developed and implemented the rotated surface code and magic state injection protocols under the supervision of MU and MS. YK carried out all experiments and plotted figures with input from MU. All authors discussed and analyzed the data. YK wrote the manuscript with input from MU and MS.

- 
- [1] Shor, P. W. Scheme for reducing decoherence in quantum computer memory. *Physical Review A* **52**, R2493–R2496 (1995). URL <https://link.aps.org/doi/10.1103/PhysRevA.52.R2493>.
- [2] Calderbank, A. R. & Shor, P. W. Good quantum error-correcting codes exist. *Physical Review A* **54**, 1098–1105 (1996). URL <https://link.aps.org/doi/10.1103/PhysRevA.54.1098>.
- [3] Steane, A. Multiple Particle Interference and Quantum Error Correction. *Proceedings of the Royal Society of London. Series A: Mathematical, Physical and Engineering Sciences* **452**, 2551–2577 (1996). URL <http://arxiv.org/abs/quant-ph/9601029>. ArXiv:quant-ph/9601029.
- [4] Terhal, B. M. Quantum error correction for quantum memories. *Reviews of Modern Physics* **87**, 307–346 (2015). URL <https://link.aps.org/doi/10.1103/RevModPhys.87.307>.
- [5] Gottesman, D. Stabilizer Codes and Quantum Error Correction (1997). URL <http://arxiv.org/abs/quant-ph/9705052>. ArXiv:quant-ph/9705052.
- [6] Bravyi, S. B. & Kitaev, A. Y. Quantum codes on a lattice with boundary (1998). URL <http://arxiv.org/abs/quant-ph/9811052>. ArXiv:quant-ph/9811052.
- [7] Dennis, E., Kitaev, A., Landahl, A. & Preskill, J. Topological quantum memory. *Journal of Mathematical Physics* **43**, 4452–4505 (2002). URL <http://arxiv.org/abs/quant-ph/0110143>. ArXiv:quant-ph/0110143.
- [8] Kitaev, A. Fault-tolerant quantum computation by anyons. *Annals of Physics* **303**, 2–30 (2003). URL <https://linkinghub.elsevier.com/retrieve/pii/S0003491602000180>.
- [9] Fowler, A. G., Whiteside, A. C. & Hollenberg, L. C. L. Towards Practical Classical Processing for the Surface Code. *Physical Review Letters* **108**, 180501 (2012). URL <https://link.aps.org/doi/10.1103/PhysRevLett.108.180501>.
- [10] Zhao, Y. *et al.* Realization of an Error-Correcting Surface Code with Superconducting Qubits. *Physical Review Letters* **129**, 030501 (2022). URL <https://link.aps.org/doi/10.1103/PhysRevLett.129.030501>.
- [11] Krinner, S. *et al.* Realizing repeated quantum error correction in a distance-three surface code. *Nature* **605**, 669–674 (2022). URL <https://www.nature.com/articles/s41586-022-04566-8>.
- [12] Google Quantum AI *et al.* Suppressing quantum errors by scaling a surface code logical qubit. *Nature* **614**, 676–681 (2023). URL <https://www.nature.com/articles/s41586-022-05434-1>.
- [13] Acharya, R. *et al.* Quantum error correction below the surface code threshold (2024). URL <http://arxiv.org/abs/2408.13687>. ArXiv:2408.13687 [quant-ph].
- [14] Berthussen, N. *et al.* Experiments with the 4D Surface Code on a QCCD Quantum Computer (2024). URL <http://arxiv.org/abs/2408.08865>. ArXiv:2408.08865 [quant-ph].
- [15] Bluvstein, D. *et al.* Logical quantum processor based on reconfigurable atom arrays. *Nature* **626**, 58–65 (2024). URL <https://www.nature.com/articles/s41586-023-06927-3>.
- [16] Reichardt, B. W. Quantum Universality from Magic States Distillation Applied to CSS Codes. *Quantum Information Processing* **4**, 251–264 (2005). URL <http://link.springer.com/10.1007/s11228-005-7654-8>.
- [17] Litinski, D. A Game of Surface Codes: Large-Scale Quantum Computing with Lattice Surgery. *Quantum* **3**, 128 (2019). URL <http://arxiv.org/abs/1808.02892>. ArXiv:1808.02892 [quant-ph].
- [18] Chamberland, C. & Campbell, E. T. Universal Quantum Computing with Twist-Free and Temporally Encoded Lattice Surgery. *PRX Quantum* **3**, 010331 (2022). URL <https://link.aps.org/doi/10.1103/PRXQuantum.3.010331>.
- [19] Eastin, B. & Knill, E. Restrictions on Transversal Encoded Quantum Gate Sets. *Physical Review Letters* **102**, 110502 (2009). URL <https://link.aps.org/doi/10.1103/PhysRevLett.102.110502>.
- [20] Erhard, A. *et al.* Entangling logical qubits with lattice surgery. *Nature* **589**, 220–224 (2021). URL <http://arxiv.org/abs/2006.03071>. ArXiv:2006.03071 [quant-ph].
- [21] Ryan-Anderson, C. *et al.* Implementing Fault-tolerant Entangling Gates on the Five-qubit Code and the Color Code (2022). URL <http://arxiv.org/abs/2208.01863>. ArXiv:2208.01863 [quant-ph].
- [22] Kim, Y., Sevier, M. & Usman, M. Transversal CNOT gate with multi-cycle error correction (2024). URL <http://arxiv.org/abs/2406.12267>. ArXiv:2406.12267 [quant-ph].
- [23] Hetényi, B. & Wootton, J. R. Creating entangled logical qubits in the heavy-hex lattice with topological codes (2024). URL <http://arxiv.org/abs/2404.15989>. ArXiv:2404.15989 [quant-ph].
- [24] Paetznick, A. *et al.* Demonstration of logical qubits and repeated error correction with better-than-physical error rates (2024). URL <http://arxiv.org/abs/2404.02280>. ArXiv:2404.02280 [quant-ph].
- [25] Ryan-Anderson, C. *et al.* High-fidelity and Fault-tolerant Teleportation of a Logical Qubit using Transversal Gates and Lattice Surgery on a Trapped-ion Quantum Computer (2024). URL <http://arxiv.org/abs/2404.16728>. ArXiv:2404.16728 [quant-ph].



- [26] Bravyi, S. & Kitaev, A. Universal quantum computation with ideal Clifford gates and noisy ancillas. *Physical Review A* **71**, 022316 (2005). URL <https://link.aps.org/doi/10.1103/PhysRevA.71.022316>.
- [27] Egan, L. *et al.* Fault-tolerant control of an error-corrected qubit. *Nature* **598**, 281–286 (2021). URL <https://www.nature.com/articles/s41586-021-03928-y>.
- [28] Postler, L. *et al.* Demonstration of fault-tolerant universal quantum gate operations. *Nature* **605**, 675–680 (2022). URL <https://www.nature.com/articles/s41586-022-04721-1>.
- [29] Ye, Y. *et al.* Logical Magic State Preparation with Fidelity beyond the Distillation Threshold on a Superconducting Quantum Processor. *Physical Review Letters* **131**, 210603 (2023). URL <https://link.aps.org/doi/10.1103/PhysRevLett.131.210603>.
- [30] Gupta, R. S. *et al.* Encoding a magic state with beyond break-even fidelity. *Nature* **625**, 259–263 (2024). URL <https://www.nature.com/articles/s41586-023-06846-3>.
- [31] McEwen, M., Bacon, D. & Gidney, C. Relaxing Hardware Requirements for Surface Code Circuits using Time-dynamics. *Quantum* **7**, 1172 (2023). URL <http://arxiv.org/abs/2302.02192>. ArXiv:2302.02192 [quant-ph].
- [32] Benito, C., López, E., Peropadre, B. & Bermudez, A. Comparative study of quantum error correction strategies for the heavy-hexagonal lattice (2024). URL <http://arxiv.org/abs/2402.02185>. ArXiv:2402.02185 [quant-ph].
- [33] Chamberland, C., Zhu, G., Yoder, T. J., Hertzberg, J. B. & Cross, A. W. Topological and Subsystem Codes on Low-Degree Graphs with Flag Qubits. *Physical Review X* **10**, 011022 (2020). URL <https://link.aps.org/doi/10.1103/PhysRevX.10.011022>.
- [34] Kim, Y., Kang, J. & Kwon, Y. Design of quantum error correcting code for biased error on heavy-hexagon structure. *Quantum Information Processing* **22**, 230 (2023). URL <https://link.springer.com/10.1007/s11128-023-03979-2>.
- [35] McLauchlan, C., Gehér, G. P. & Moylett, A. E. Accommodating Fabrication Defects on Floquet Codes with Minimal Hardware Requirements (2024). URL <http://arxiv.org/abs/2405.15854>. ArXiv:2405.15854 [quant-ph].
- [36] Wang, D. S., Fowler, A. G., Stephens, A. M. & Hollenberg, L. C. L. Threshold error rates for the toric and surface codes (2009). URL <http://arxiv.org/abs/0905.0531>. ArXiv:0905.0531 [quant-ph].
- [37] Gidney, C. Stim: a fast stabilizer circuit simulator. *Quantum* **5**, 497 (2021). URL <http://arxiv.org/abs/2103.02202>. ArXiv:2103.02202 [quant-ph].
- [38] Higgott, O. PyMatching: A Python Package for Decoding Quantum Codes with Minimum-Weight Perfect Matching. *ACM Transactions on Quantum Computing* **3**, 1–16 (2022). URL <https://dl.acm.org/doi/10.1145/3505637>.
- [39] Higgott, O. & Gidney, C. Sparse Blossom: correcting a million errors per core second with minimum-weight matching (2023). URL <http://arxiv.org/abs/2303.15933>. ArXiv:2303.15933 [quant-ph].
- [40] Sundaresan, N. *et al.* Demonstrating multi-round subsystem quantum error correction using matching and maximum likelihood decoders. *Nature Communications* **14**, 2852 (2023). URL <https://www.nature.com/articles/s41467-023-38247-5>.
- [41] Google Quantum AI *et al.* Exponential suppression of bit or phase errors with cyclic error correction. *Nature* **595**, 383–387 (2021). URL <https://www.nature.com/articles/s41586-021-03588-y>.
- [42] IBM Quantum, and Community. *Qiskit: An open-source framework for quantum computing* (2021). URL <https://doi.org/10.5281/zenodo.2573505>.
- [43] Schmied, R. Quantum state tomography of a single qubit: comparison of methods. *Journal of Modern Optics* **63**, 1744–1758 (2016). URL <https://www.tandfonline.com/doi/full/10.1080/09500340.2016.1142018>.
- [44] B., E. & R.J., T. *An Introduction to the Bootstrap* (Chapman and Hall/CRC, 1994). URL <https://doi.org/10.1201/9780429246593>.
- [45] Fowler, A. G., Mariantoni, M., Martinis, J. M. & Cleland, A. N. Surface codes: Towards practical large-scale quantum computation. *Physical Review A* **86**, 032324 (2012). URL <https://link.aps.org/doi/10.1103/PhysRevA.86.032324>.
- [46] Gidney, C., Newman, M., Fowler, A. & Broughton, M. A Fault-Tolerant Honeycomb Memory. *Quantum* **5**, 605 (2021). URL <http://arxiv.org/abs/2108.10457>. ArXiv:2108.10457 [quant-ph].

## Appendix A: Asymmetric Feature of Threshold

Fig. 2a and b in the main text show logical error rates of Z and X errors, respectively. There is a crossover point for each logical error type, known as the threshold value ( $p_{\text{th}}$ ), where the relation between the physical error rate and the corresponding logical error rate changes: For  $p < p_{\text{th}}$ ,  $p_L$  decreases as the code distance increases, whereas for  $p > p_{\text{th}}$ ,  $p_L$  increases with the code distance. The threshold values for logical phase- ( $p_{\text{th}}^Z \approx 0.31\%$ ) and bit-flip ( $p_{\text{th}}^X \approx 0.37\%$ ) errors are distinct.

$$p_L^Z = C_Z/\Lambda_Z^{a_Z(d+1)/2}, \quad p_L^X = C_X/\Lambda_X^{a_X(d+1)/2} \quad (\text{A1})$$

To analyze further in detail, we use fitting equations (A1) describing the logical error rate of Z and X errors as  $p_L^Z(p, d)$  and  $p_L^X(p, d)$  [41]. The fitting is carried out using predefined threshold values for phase- and bit-flip errors denoted as  $p_{\text{th}}^Z$  and  $p_{\text{th}}^X$ , respectively, where  $\Lambda_Z \propto p_{\text{th}}^Z/p$  and  $\Lambda_X \propto p_{\text{th}}^X/p$ . In these formulas, the terms  $C_Z$ ,  $C_X$ ,  $a_Z$ , and  $a_X$  are fitting constants. Especially,  $a_Z$  and  $a_X$  are parameters closely relevant to the performance of the code, specifically associated with the number of errors forming a non-trivial error chain. Even in the regime where the qubit error rate is lower than a threshold, which requires exponential growth in the number of samples, these statistical arguments allow for estimating logical error rates using fitting values [13, 32, 41, 45, 46].

When the parameters ( $a_Z$  and  $a_X$ ) are set to 1, the minimum number of errors required to produce a logical error is  $\frac{d+1}{2}$  for an odd code distance  $d$ . This shows how the code can efficiently correct bit-flip and phase-flip errors. However, if these parameters are less than 1, it indicates that a logical error could occur with fewer errors. For instance, with a code distance of  $d = 3$ , at least two errors are required to cause a logical error. However, if one of the parameters is less than 1, even a single error could induce a logical error of that type, indicating the possibility of a weight-one error transforming into a weight-two error.

$$a_Z \approx 0.7, \quad a_X \approx 1$$

We obtained the fitting parameters as  $a_Z \approx 0.7$  and  $a_X \approx 1$ . While the code for correcting logical X errors maintains the effectiveness of code distance, it is biasedly vulnerable to logical Z errors. We note the asymmetric property in correcting the two types of errors, even under the unbiased noise model. We attributed this property to error propagation among data qubits.

When layers of CNOT gates are implemented in a sub-round syndrome extraction circuit, errors on data qubits can spread through the gates. Crucially, this error propagation occurs, propagating an error from one data qubit to its vertically adjacent neighbor rather than a horizontally neighboring data qubit. Error propagation in the

horizontal direction is restricted because of either the existence of syndrome qubits or the constraints of direct interaction. In contrast, errors can propagate vertically owing to the process for (un)folding stabilizers requiring long-range CNOT gates among vertically neighboring data qubits. This directional limitation on error propagation affects the efficiency of the code correcting errors, as a weight-one error can escalate into a weight-two error. It is important to note that the detrimental impact is particularly significant for a logical error that coincides with the direction of data qubits associated with the logical operator, weakening the code's error-correction capability in such cases. In our case, vertical error propagation hampers the correction of a logical error defined vertically, which is the logical Z operator. Therefore, Error propagation among data qubits causes ambiguity in calculating a correction operator and a lower error threshold decreasing the effective code distance.

## Appendix B: Expectation values

Fig. 5a shows experimentally estimated logical expectation values of logical Pauli operators. The values are estimated from the samples producing the trivial syndrome obtained by sampling  $2 \times 10^4$  times for logical measurements in each Pauli basis. Their ideal values can be expressed in terms of polar( $\theta$ ) and azimuthal( $\phi$ ) angles as shown in Fig. 5b:

$$\langle \psi_L | \hat{X}_L | \psi_L \rangle = \sin\theta \cos\phi \quad (\text{B1})$$

$$\langle \psi_L | \hat{Y}_L | \psi_L \rangle = \sin\theta \sin\phi \quad (\text{B2})$$

$$\langle \psi_L | \hat{Z}_L | \psi_L \rangle = \cos\theta \quad (\text{B3})$$

Although experimental results range approximately from  $-0.6$  to  $0.6$  for logical X and Y operators and around  $-0.8$  to  $0.8$  for the logical Z operator, their theoretical values vary from  $-1$  to  $1$ . However, we find that the experimental results closely align with the ideal values.

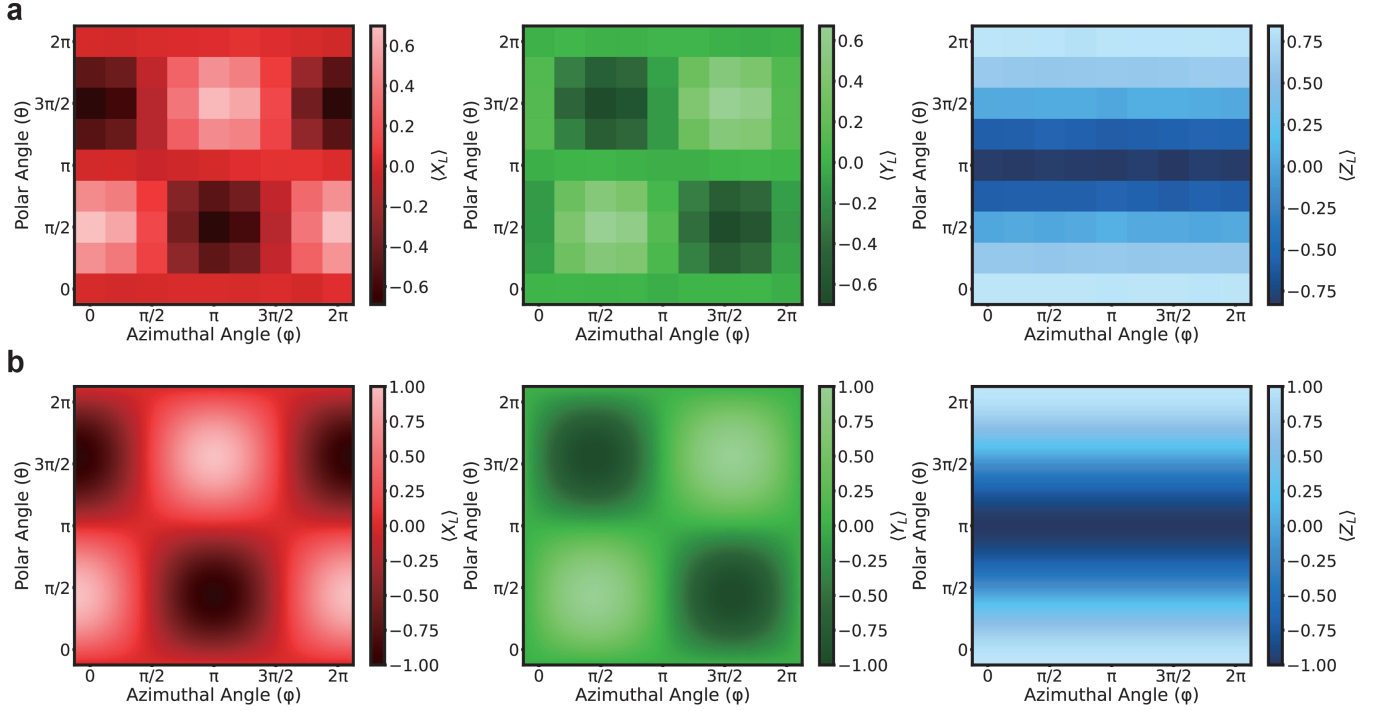


FIG. 5: **Expectation values.** **a.** The expectation values of logical Pauli operators  $X$ ,  $Y$ , and  $Z$  in raw logical magic states prepared on `ibm_fez` device. These values are plotted on a plane with the polar ( $\theta$ ) and azimuthal( $\phi$ ) angles, ranging from 0 to  $2\pi$ . **b.** Their theoretical values are plotted as functions of parameters  $\theta$  and  $\phi$  as expressed in (B1), (B2), and (B3).

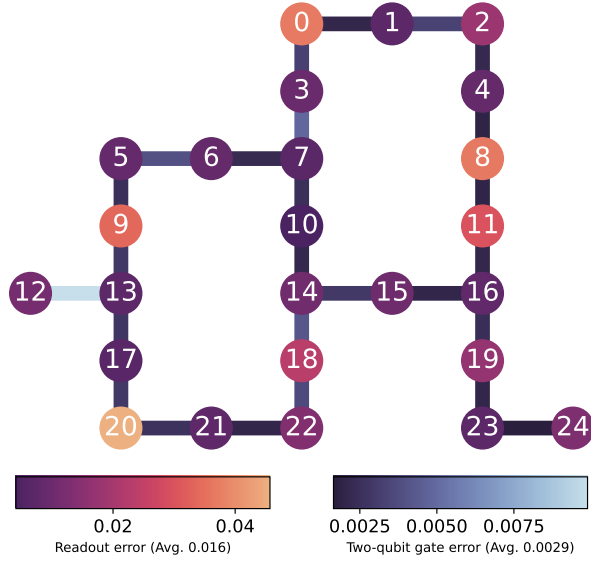


FIG. 6: Hardware specifications of physical qubits on `ibm_fez` for magic state injection. The graph shows the chosen physical qubits' specifications of the distance-3 rotated surface code onto the heavy-hexagon structure. Each node and edge correspond to the physical qubit and the connectivity of a two-qubit gate (CZ). The error rates of readout and two-qubit gate are displayed with colors. Their average error rate are  $1.6 \times 10^{-2}$  and  $2.9 \times 10^{-3}$ .